processes

MDPI

Article

The Numerical Analysis of Non-Newtonian Blood Flow in a Mechanical Heart Valve

Aolin Chen [1], Adi Azriff Basri [2], Norzian Bin Ismail [3] and Kamarul Arifin Ahmad [2,4,*]

[1] Department of Mechanical Engineering, Faculty of Engineering, University Putra Malaysia, Serdang 43400, Selangor, Malaysia
[2] Department of Aerospace Engineering, Faculty of Engineering, University Putra Malaysia, Serdang 43400, Selangor, Malaysia
[3] Department of Medicine, Faculty of Medicine and Health Sciences, University Putra Malaysia, Serdang 43400, Selangor, Malaysia
[4] Aerospace Malaysia Research Center (AMRC), Faculty of Engineering, University Putra Malaysia, Serdang 43400, Selangor, Malaysia
* Correspondence: aekamarul@upm.edu.my

Abstract: Background: The non-physiological structure of mechanical heart valves (MHVs) affects the blood flow field, especially the complex microstructure at the hinge. Numerous studies suggest that the blood flow field in the aortic area with an MHV can be considered Newtonian. However, the Newtonian assumption is occasionally unreasonable, where blood viscosity changes with shear rate, exhibiting non-Newtonian shear-thinning characteristics. Methods: In this research, a comprehensive study of the non-Newtonian effects on the hemodynamic behavior of MHVs was performed. The impact of the Newtonian hypothesis was investigated on the internal hemodynamics of MHVs. Several non-Newtonian and Newtonian models were used to analyze the chamber flow and blood viscosity. MHVs were modeled and placed in simplified arteries. After the unstructured mesh was generated, a simulation was performed in OpenFOAM to analyze its hemodynamic parameters. Results: In the study of the non-Newtonian viscosity model, the Casson model differs significantly from the Newtonian model, resulting in a 70.34% higher wall shear stress. In the modified Cross and Carreau models, the non-Newtonian behavior can significantly simulate blood in the MHV at different stages during initial and intermediate deceleration. The narrowing of the hinge region in particular, has a significant impact on evaluating blood rheology. The low flow rate and high wall shear force at the hinge can cause blood cell accumulation and injury time, resulting in hemolytic thrombosis. Conclusion: The results exhibit that the Newtonian hypothesis underestimates the hemodynamics of MHVs, whose complex structure leads to increased recirculation, stagnation, and eddy current structure, and a reasonable choice of blood viscosity model may improve the result accuracy. Modfied Cross and Carreau viscosity models effectively exhibit the shear-thinning behavior in MHV blood simulations.

Keywords: mechanical heart valve; non-Newtonian viscosity model; wall shear stress; computational fluid dynamics

check for updates

Citation: Chen, A.; Basri, A.A.; Ismail, N.B.; Ahmad, K.A. The Numerical Analysis of Non-Newtonian Blood Flow in a Mechanical Heart Valve. *Processes* **2023**, *11*, 37. https://doi.org/10.3390/pr11010037

Academic Editor: Udo Fritsching

Received: 30 November 2022
Revised: 19 December 2022
Accepted: 21 December 2022
Published: 24 December 2022

1. Introduction

Heart valve disease is a cardiovascular disease that is one of the leading causes of death worldwide [1]. Hundreds of thousands of heart valves are implanted annually [2,3]. Mechanical heart valves (MHVs) are the most commonly used type of valve for replacement surgery due to their ideal hemodynamic properties and durability [4]. However, MHV-induced non-physiological blood flow increases the risk of hemolysis, platelet activation, and thromboembolism [5,6].

Blood includes complex components, such as cells, proteins, and ions. When the blood is subjected to low amounts of shear stress, the components aggregate and form

rouleaux, resulting in non-Newtonian viscosity. The shear rate has a significant impact on blood viscosity. The shear rate during the transition period is approximately 100 s^{-1} for non-Newtons and Newtons. The Newtonian hypothesis is valid when the blood viscosity remains constant beyond the transition period [7]. The pulsatile blood flow with wide ranges of shear rate in arteries. Several studies assume that blood is an incompressible Newtonian fluid [2,3,8] and state that the non-Newtonian viscosity can be ignored when the vessel diameter is larger than 0.5 mm. In the aorta, the blood with a wide range of shear rates, certain aortic conditions induce disturbance of blood flow, which can significantly reduce the shear rate [9]. Large shear rates and a pulsatile, transitional nature characterize the blood flow in the aorta. Therefore, the blood's effective viscosity becomes asymptotically constant in these larger vessels. This flow is inhomogeneous; therefore, the assumption of a Newtonian fluid is partially accurate. However, the blood exhibits non-Newtonian behavior, specifically shear-thinning properties at low shear stresses [10–12]. These characteristics are particularly evident during the cardiac cycle when the mean flow rate is low and the shear rate is correspondingly reduced, leading to the generation of recirculation and resident regions even at high flow rates. An MHV implant may induce the non-physiological blood flow. Recirculating, stagnant, vortex, and flow separation are common structures downstream of an MHV [7,13,14], enhancing low shear rates and motivating non-Newtonian modeling. The leaflet gaps and hinge region have complex and small size structures in an MHV, the microflow would induce a broad range of shear stress, and the microstructure sizes are comparable to red blood cells. Non-Newtonian assumptions describing shear-thinning blood characteristics may be more accurate when the feature-length becomes sufficiently small [13].

Blood viscosity is a critical factor in generating shear stresses [15]. Various models have been proposed to describe blood's non-Newtonian, shear-thinning, and viscoelastic properties [16]. The Carreau [17–19] and Carreau–Yasuda [20] models are commonly used in the literature. The Carreau–Yasuda model is often used to describe the non-Newtonian behavior of blood due to its ability to accurately capture viscosity changes [18,21–23]. They also suggested that this model can be used in numerical simulations of non-Newtonian blood flow in the MHV model. Abbas et al. [24] investigated the platelet activation potential of blood in the MHV model using the Carreau–Yasuda non-Newtonian model. Chaos et al. [25] compared Newtonian and non-Newtonian blood flow properties and discovered that blood flow is similar, but the non-Newtonian model produced higher shear stress. Mirkhani et al. [23] and De Vita et al. [18] studied the characteristics of blood in the hinge region of the MHV under the non-Newtonian model. They discovered that the wall shear stress between the two leaflets has a great influence [26]. The leaflet gaps and hinge regions experience a wide range of shear stresses in the MHV model, making it necessary to consider the non-Newtonian behavior of blood in these regions for realistic results [23]. However, many MHV simulations simplify the vessel's structure, neglecting the details of the hinge region to accelerate the simulation. This simplification may underestimate the stresses experienced by blood elements, making the model less accurate in predicting the hemolysis risk [15]. Most literature indicates that the non-Newtonian behavior of blood is a critical factor that primarily affects the prediction of cardiovascular hemodynamics.

The non-Newtonian viscosity property affects the flow characteristics and assumption for wall shear stress, as many researchers used the Carreau [25] and Carreau–Yasuda [23] models in the MHV simulation. Most of the current research on MHV blood simulation is limited to a Newtonian or single non-Newtonian viscosity model, which is insufficient to study the difference between various non-Newtonian shear-thinning models and their impact on the simulation results. Several studies have compared the performance of different non-Newtonian viscosity models at the carotid bifurcation [27–29], the aortic arch [30], and in continuous narrowed arteries [31]. These studies have demonstrated that various non-Newtonian models can produce different results for axial velocity values [32] and wall shear stress (WSS) [33]. Based on the existing research, no researchers have studied

different non-Newtonian models of hemodynamic behavior affected by MHV. The present study examines the impact of 10 different non-Newtonian viscosity models on specific hemodynamic features in the MHV model with aortic sinus during the systole stage of the cardiac cycle. MHV geometry simplification has been avoided, which means that the hinge region was retained.

This study presents a computational methodology for simulating blood flow in the On-x MHV model. The methodology includes a description of the MHV structure, the governing equations used to model blood flow, and the hemorheological properties of blood. Different non-Newtonian and Newtonian viscosity models are introduced and compared using parameters such as flow velocity and wall shear stress. These comparative results are used to study the differences between non-Newtonian and Newtonian models to identify the most suitable model for simulating non-Newtonian blood flow in the MHV.

2. Methods

The construction of the MHV model is demonstrated in this section. The numerical method, boundary conditions, and governing equations are also discussed.

2.1. Geometry

The 23 mm On-X heart valve, one of the most promising BMHVs, was utilized in this study. The model was created using SolidWorks software, and the structural data was generated from Mirkhani et al. [34]. The data was obtained using optical three-dimensional (3D) scanning equipment, and the sewing ring was removed, but maintained the hinge area recess and leaflets ear. The non-symmetric and butterfly-shaped hinge region model and the zooming in this region are illustrated in Figure 1.

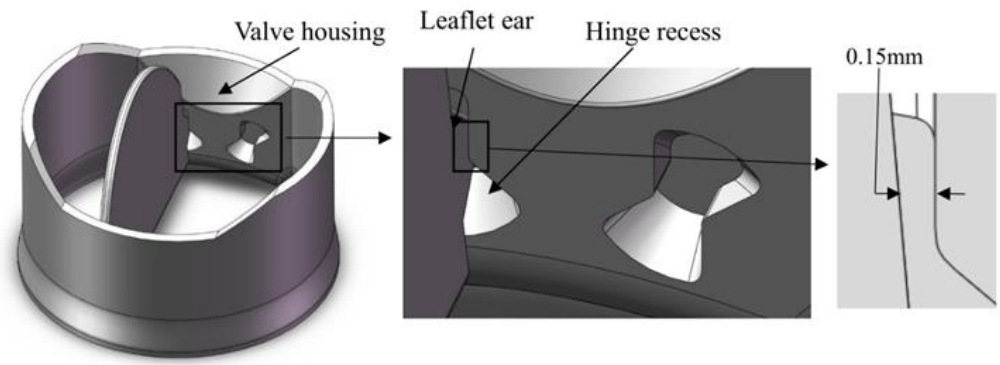

Figure 1. Hinge recess and leaflet ear of the modeled On-X valve.

There are gaps between the different parts of the MHV model and their presence can cause significant shearing of blood cells flowing through this area. Significant shear stress can be detected in the hinge area where the leaflet hinge and valve housing contact. The shear stress makes the blood more prone to complications such as hemolysis and platelet activation in this area. Due to the high computational costs involved, a properly optimized model with a minimum clearance of 0.15 mm in the hinge area is necessary. Figure 2 depicts a structural diagram of a 3D MHV with a physiological aortic root. The valve was connected to a realistic aortic root consisting of three sinuses of Valsalva. The three sinuses of Valsalva were placed in equally spaced radial positions, reproducing the model used in a previous study [35].

Figure 2. Fluid domain inside the ascending aorta of an MHV.

Our study concentrates on the heart systole stage and keeps the valve leaflet fully open. Figure 3 displays the open angle for the On-x valve leaflet free rotation angle, 40° $(fully\ closed)$ to 90° $(fully\ open)$ [36]. However, previous research has displayed that the MHV creates a nozzle-like shape that accelerates blood flow through, and the pressure may be increased in the middle diffuser-shaped orifice to balance the impact of flow induced and make the leaflet flutter at approximately an 85° position [34]. Thus, the valve leaflet was kept at 85° (Figure 4) and the cross-sectional view was cut through two midplanes perpendicular to the valve.

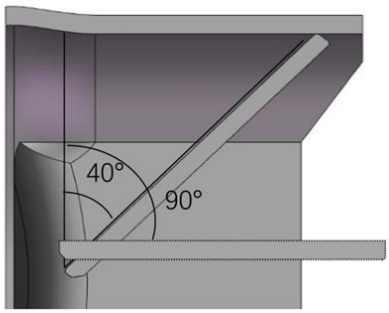

Figure 3. An MHV leaflet fully open (90°) and fully closed (40°).

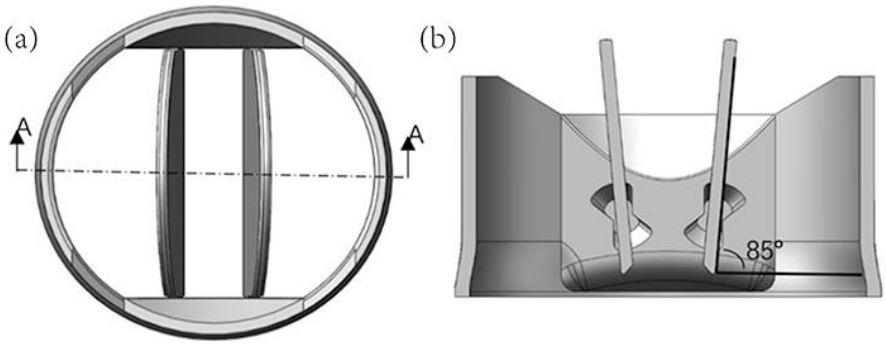

Figure 4. The leaflet angle at the fully open position (**a**) Top viw of MHV, (**b**) Cutaway view of MHV.

2.2. Governing Equation

The OpenFOAM open-source toolbox with the pimpleFoam unsteady incompressible solver was used in this study. The pimpleFoam is a combination of the PISO and SIMPLE algorithms [37]. The blood is assumed to be an incompressible fluid with the equation of continuity and momentum as follows:

$$\nabla \cdot \mathbf{U} = 0 \tag{1}$$

$$\frac{\partial(\rho \mathbf{U})}{\partial t} + \nabla \cdot (\rho \mathbf{U}\mathbf{U}) - \nabla \cdot (\mu \nabla \mathbf{U}) - (\nabla \mathbf{U}\mathbf{U}) \cdot \nabla \mu = -\nabla p \tag{2}$$

where **U** represents the velocity vector, p represents pressure, μ represents viscosity, and ρ represents density. The fluid was considered an incompressible fluid with a den-

sity $\rho = 1060\ \mathrm{kg/m^3}$. When assuming blood as Newtonian, the kinematic viscosity is $v = 3.3^{-6}\mathrm{m^2/s}$. The governing equation is based on an OpenFOAM solver [38]. The pimpleFoam solvers in OpenFOAM can automatically adjust the time step: the time step is set as $1e^{-6}$, open the adjustTimeStep function, and set maxCo as 1 to limit the timestep adjustment. The PIMPLE algorithm flow is shown in Figure 5. The predicted speed $\mathbf{U}^*$ was solved, according to the initial conditions, $\mathbf{HybA}^*$ was constructedthrough the equation, then the pressure p was solved, $\mathbf{U}^{**}$ was updated according to $\mathbf{HybA}^*$ and p, to determine whether the iterative solution was performed according to the conditions, and finally, the PISO inner loop was completed. Following this, it was estimated whether the SIMPLE cycle was finished according to the outer loop condition, a PIMPLE solution was completed, and the time step started the next cycle: where: $\mathrm{A_P} = 1/\Delta\mathrm{t} + 1/\mathrm{V_P}\sum(\mathrm{F_f^t}/2) + (1/\mathrm{V_P})\sum \mathrm{v}(|\mathbf{S_f}|/|\mathbf{d}|)$, $\mathrm{A_N} = -1/\mathrm{V_P}(\mathrm{F_f^t}/2 - v(|\mathbf{S_f}|/|\mathbf{d}|)$, and $\mathrm{S_P^t} = (1/\Delta\mathrm{t})\mathbf{U_P^t}$. The superscript t represents the current time step (known), the superscript $*$ represents the prediction step (to be determined), the subscript f represents the value on the grid cell surface, denotes the vector difference (distance vector) between the body centers of the grid cells, the subscript N denotes the velocity of the neighboring grid cells, and the subscript p denotes the velocity of the current grid cell. v represents the dynamic viscosity $\mathrm{V_p}$ represents the grid cell volume, $\mathbf{S_f}$ represents the face vector of each face of the grid cell, and $\mathrm{F_f^t}$ is the flux.

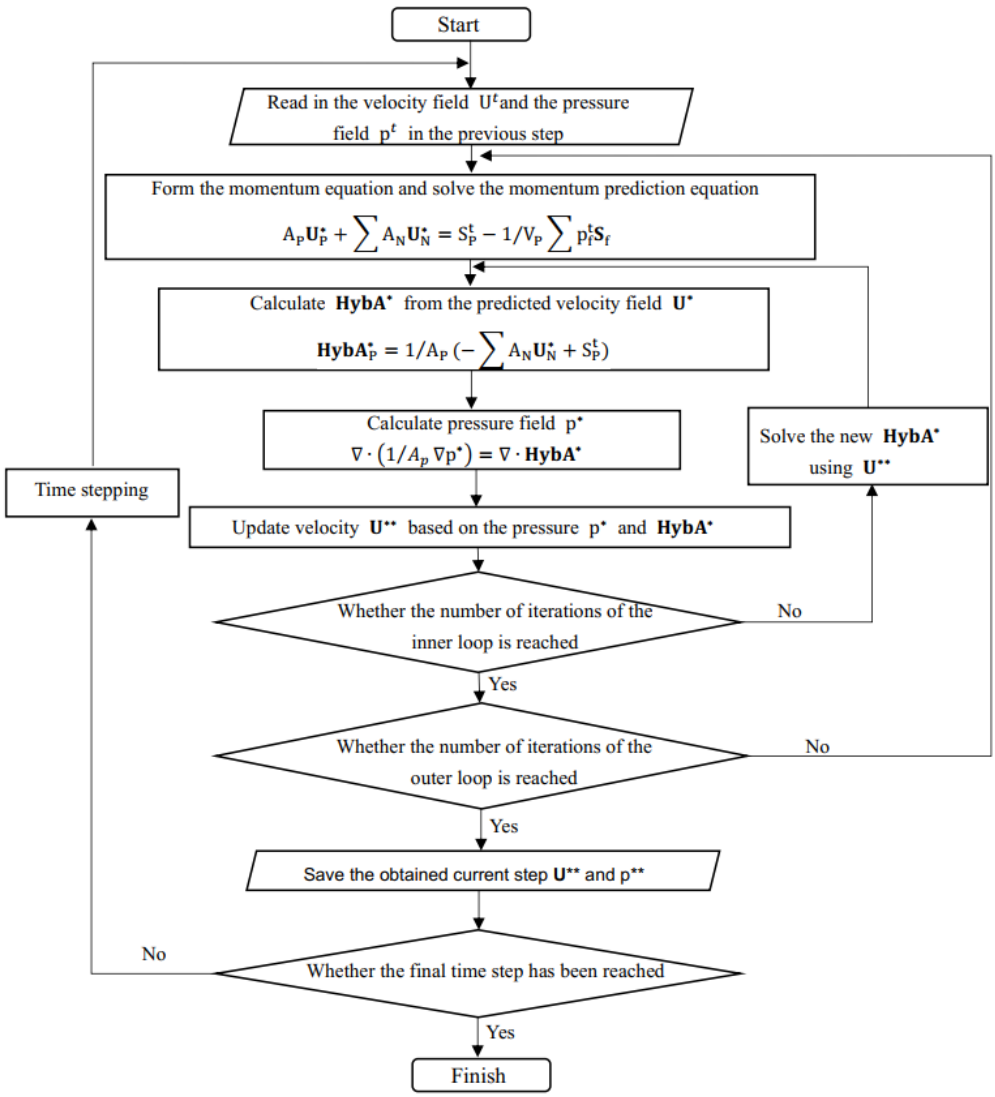

Figure 5. The basic steps of the PIMPLE algorithm solution.(The superscript * represents the prediction step (to be determined)).

2.3. Non-Newtonian Blood Rheologies

Newtonian and different non-Newtonian models were used to study fluid behaviors. These non-Newtonian models were commonly used to describe shear-thinning viscosity characteristics. Table 1 defines 10 non-Newtonian constitutive viscosity equations with corresponding parameters. Figure 6 shows viscosity versus strain rate for the different models. The changes in the rheological model differ at different time intervals. Excluding the power-law model, when the shear rate is less than 100 s^{-1}, the viscosity of the non-Newtonian models presents different change curves, but the viscosity is significantly higher than the Newtonian viscosity. When the shear rate exceeds 10^3 s^{-1}, the shear rate increases. The non-Newtonian models' viscosity values are very close to Newtonian viscosity.

Table 1. Non-Newtonian viscosity models of blood flow.

Model	Viscosity	Parameters
Modified Power-law (PL) [39]	$\eta_\infty < \eta(\dot{\gamma}) = k(\dot{\gamma})^{n-1} < \eta_0$	$k = 0.017$ $n = 0.708$ $\eta_0 = 0.056$ Pas $\eta_\infty = 0.0035$ pas
Carreau [25]	$\eta(\dot{\gamma}) = \eta_\infty + (\eta_0 - \eta_\infty)\left[1 + (\lambda\dot{\gamma})^2\right]^{\frac{n-1}{2}}$	$\eta_0 = 0.056$ Pas $\eta_\infty = 0.0035$ Pas $\lambda = 3.313005$ $n = 0.3568$
Carreau–Yasuda (CY) [40]	$\eta(\dot{\gamma}) = \eta_\infty + (\eta_0 - \eta_\infty)\left[1 + (\lambda\dot{\gamma})^a\right]^{\frac{n-1}{a}}$	$\eta_0 = 0.056$ Pas $\eta_\infty = 0.0035$ Pas $\lambda = 8.2$ $n = 0.2128$ $a = 0.64$
Casson [16]	$\eta(\dot{\gamma}) = \left((\sqrt{\eta_c} + \sqrt{\frac{\tau_C}{\dot{\gamma}}}\right)^2$	$\eta_c = 0.00414$ $\tau_c = 0.0038$
Modified Casson [7]	$\eta(\dot{\gamma}) = \left(\sqrt{\eta_c} + \frac{\sqrt{\tau_c}}{\sqrt{\lambda}+\sqrt{\dot{\gamma}}}\right)^2$	$\eta_c = 0.002982$ $\tau_c = 0.02876$ $\lambda = 4.020$
Cross [21]	$\eta(\dot{\gamma}) = \eta_\infty + \frac{\eta_0 - \eta_\infty}{1+(\lambda\dot{\gamma})^a}$	$\eta_0 = 0.0364$ Pas $\eta_\infty = 0.0035$ Pas $\lambda = 0.38$ s $a = 1.45$
Modified Cross [21]	$\eta(\dot{\gamma}) = \eta_\infty + \frac{\eta_0 - \eta_\infty}{(1+(\lambda\dot{\gamma})^a)^n}$	$\eta_0 = 0.056$ Pas $\eta_\infty = 0.0035$ Pas $\lambda = 3.736$ s $a = 2.406$ $n = 0.254$
Powell–Eyring (PE) [41]	$\eta(\dot{\gamma}) = \eta_\infty + (\eta_0 - \eta_\infty)\left[\frac{\sinh^{-1}(\lambda\dot{\gamma})}{\lambda\dot{\gamma}}\right]$	$\eta_0 = 0.056$ Pas $\eta_\infty = 0.0035$ Pas $\lambda = 5.383$ s
Modified Powell–Eyring (Md PE) [41]	$\eta(\dot{\gamma}) = \eta_\infty + (\eta_0 - \eta_\infty)\left[\frac{\ln(\lambda\dot{\gamma}+1)}{(\lambda\dot{\gamma})^n}\right]$	$\eta_0 = 0.056$ Pas $\eta_\infty = 0.0035$ Pas $\lambda = 2.415$ s $n = 1.05$
K–L [42]	$\eta(\dot{\gamma}) = \left(\frac{1}{\dot{\gamma}}\right)\left(\tau_C + \eta_C\left(\alpha_2\sqrt{\dot{\gamma}} + \alpha_1\dot{\gamma}\right)\right)$	$\eta_c = 0.0035$ $\tau_c = 0.005$ $\alpha_1 = 1$ $\alpha_2 = 1.19523$

The viscosity model has two other main types. The first is the shear-dependent type which can be described as Equation (3):

$$\eta = \eta_\infty + (\eta_0 - \eta_\infty)\cdot F(\dot{\gamma}) \tag{3}$$

where η_0 and η_∞ are the asymptotic viscosity values at zero and infinite shear rates, respectively, while $F(\dot{\gamma})$ is the shear-dependent function. Different choices of the function $F(\dot{\gamma})$ correspond to different blood flow models. This type includes Cross, Modified Cross, Carreau, Carreau–Yasuda, Powell–Eyring, and modified Powell–Eyring models. The Carreau

non-Newtonian model theoretical value approximates the experimental, but does not over-predict the non-Newtonian effects [30]. The Cross model is similar to the Carreau–Yasuda. It is modified by introducing a transition parameter [40]. The Powell–Eyring model is complex, but has some advantages: it is derived from kinetic theory and the Powell–Eyring fluid reduces to Newtonian fluid at low and high shear rates.

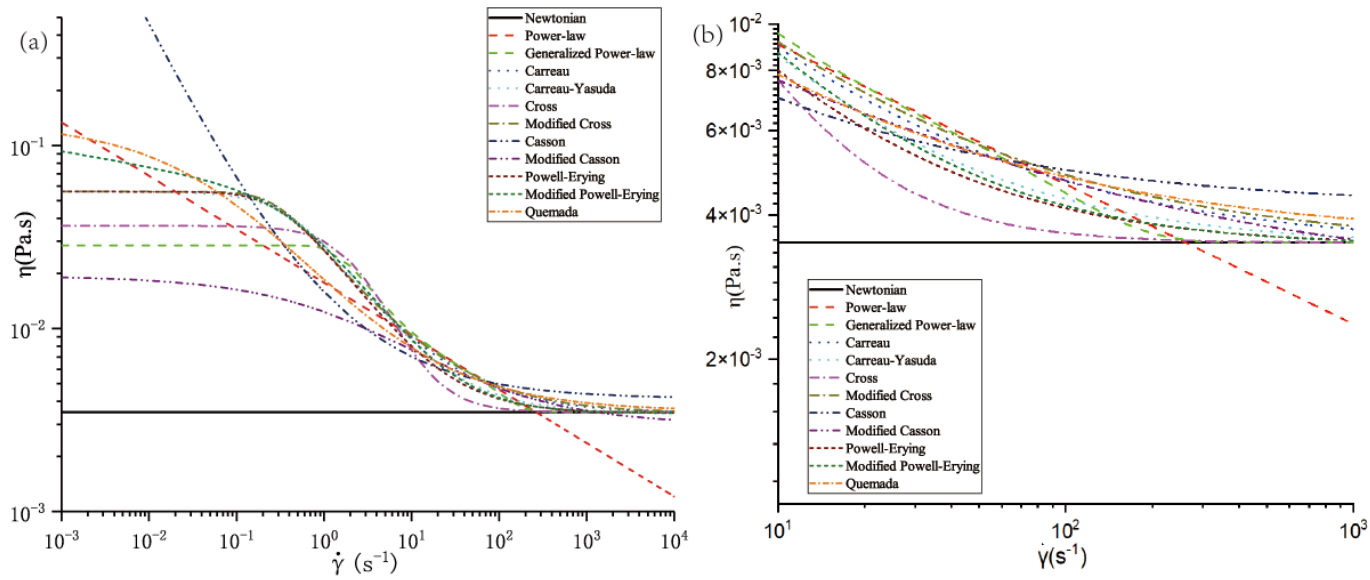

Figure 6. (**a**) Viscosity for different rheological models with (**b**) details of the zone of interest.

The other is the yield stress type. When the shear stress is below the threshold, the characteristics behave like a solid. K–L, Casson, and Modified Casson are typical yield stress-type non-Newtonian viscosity models. The viscosity is infinite at a zero shear rate, while zero is at an infinite shear rate. The K–L and Modified Casson models are modified from the Casson model and include additional shear rate modifiers. The K–L model can describe a wider shear range of w with an accuracy consistent with the experimental data.

2.4. The Simulation Method

The fluid boundary conditions were derived from previous numerical simulations of the flow through the MHV in an aortic physical environment [43] and enforced typical physical flow conditions of approximately 25 L/min peak flow rate and a 0.86 s cardiac cycle, one-third of which is systolic length. The inlet velocity was prescribed using the given waveforms. Due to the limitation of computing resources, the simulation was conducted only on the systolic duration and the leaflet was retained in the completely open position, see Figure 7, with the leaflet open-angle fixed at 85° in its fully-open position. There were four time instants within the systolic stage:

$T_1 = 0.03$ s, the early accelerating phase;
$T_2 = 0.09$ s, mid-acceleration phase;
$T_3 = 0.19$ s, peak systole;
$T_4 = 0.29$ s, mid-decelerating phase.

The fluid domain was subdivided into 593,818tetrahedral elements to ensure enough nodes to capture the main flow features, requiring approximately 18 h per simulation on a workstation with two Intel Platinum 8171M 3Ghz-processors and 128 GB of RAM.

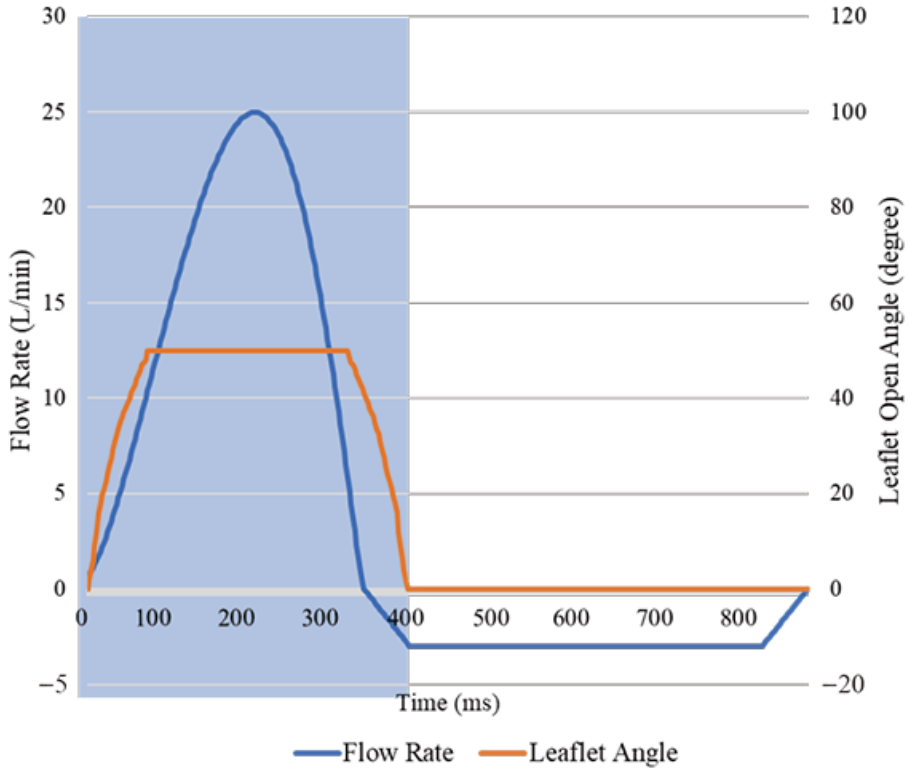

Figure 7. Flow rate pulse of the aorta inlet with the leaflet open angle changes [44].

Unstructured tetrahedral mesh technology was used for mesh division and performing densification processing at hinge regions and leaflets to improve the resolution of key parts and obtain high-precision results. Figure 8 presents the grid structure of the computational domain. Five grid sets were used to perform grid-independent studies at peak systole. Grid-independent studies were performed using different grid sizes from 1,206,722 to 3,379,553 (Figure 9). It is not difficult to verify grid-independent velocities in grid-independent verification, but achieving grid independence in the computed WSS fields requires more nodes and may show errors even on grids that generate grid-independent velocity fields [45]. The WSS is obtained on the wall, and the results indicate that when the number of grids exceeds three million, the WSS does not increase significantly. The error is less than 2%. Three million grids were used in this study.

Figure 8. Computational mesh.

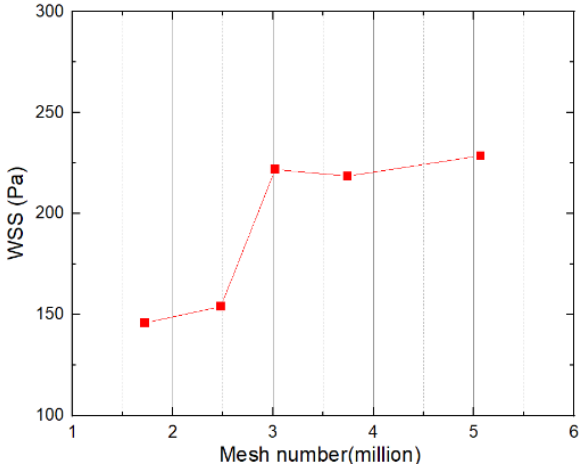

Figure 9. Grid independency study (WSS vs. mesh number).

The normalized velocity distribution curve 7 mm downstream of the valve during peak systole is displayed in Figure 10. The similar geometry illustrates the velocity fractures obtained by similar aggregate shapes and flow conditions [46,47]. When the stable output reached 7 L/min, the maximum velocity was compared. In this study, the maximum velocity was 1.44 m/s, the same as the previously reported maximum velocity of 1.36 m/s was equivalent [46]. The maximum speed difference was less than 6%, indicating that this research is consistent with the measured value.

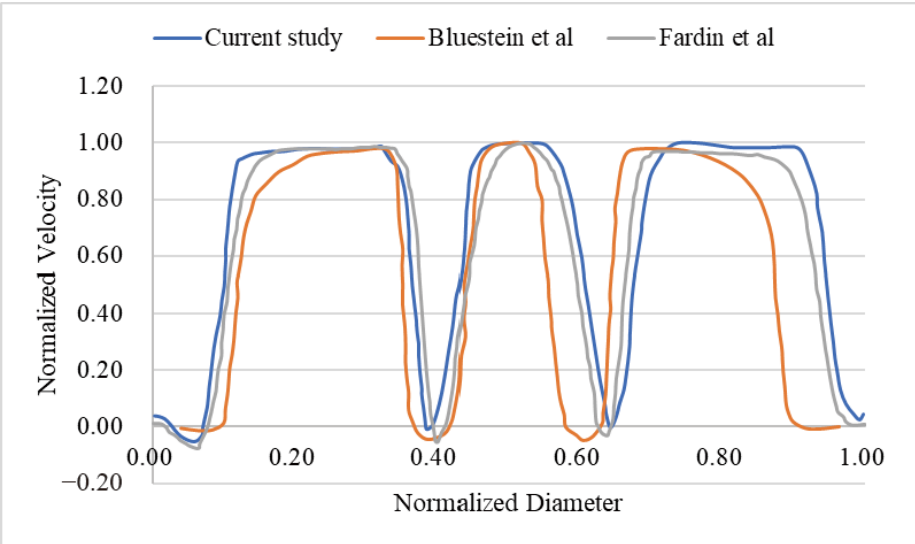

Figure 10. Normalized velocity curves on the centerline behind the leaflet in the current study compared to previous experiments [46] and calculations [47].

3. Results and Discussion

3.1. The Blood Flow Pattern

Blood should be maintained in artificial medical engineering methods in laminar flow to reduce energy loss and blood damage. Before this beneficial blood flow pattern can be satisfied, the prosthetic organ must provide as much compatibility as possible to reduce blood turbulence. Therefore, the effect of an MHV on blood flow and the importance of the non-Newtonian flow assumption is investigated by simulating the blood flow pattern through the MHV.

Figure 11a displays the peak stage velocity profile in the mid-plane passing through the On-X valve. The low-velocity blood flow filled in the sinus region, resulting in the vortex formation around this area. The triple-jet structure is visible near the valve and

gradually fades with the blood moving in the ascending aorta. To verify the diffusivity downstream of the leaflet, Figure 11b depicts a different layer of the valve downstream velocity distribution. The line from the perpendicular to the valve orientation is plotted over. Blood flow through the valve leaflet forms three jets downstream that dissipate with the flow and eventually form a complex turbulent flow.

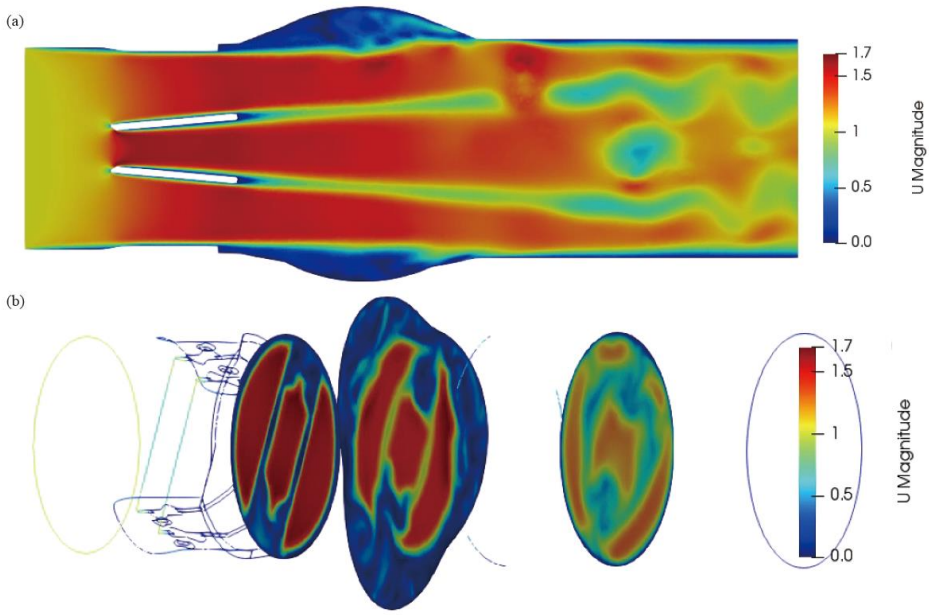

Figure 11. Peak ststolephase velocity contours (**a**) at the mid-plane (**b**) at the three planes with different distances from the valve (Newtonian model).

The velocity streamlines in the MHV shown in Figure 12. At the early acceleration phase (t = 0.03 s), the velocity streamline displays a streamlined shape. As time progresses, the velocity increases during the mid-acceleration phase (t = 0.09) leading to the formation of a typical annular vortex in the sinus region behind the leaflet. At peak velocity (t = 0.19) the leaflet and sinus region exhibit a more intense vortical structure. In the mid-decelerating phase (at t = 0.29 s), the complex vortex structure evolves into a large annular vortex structure within the sinus.

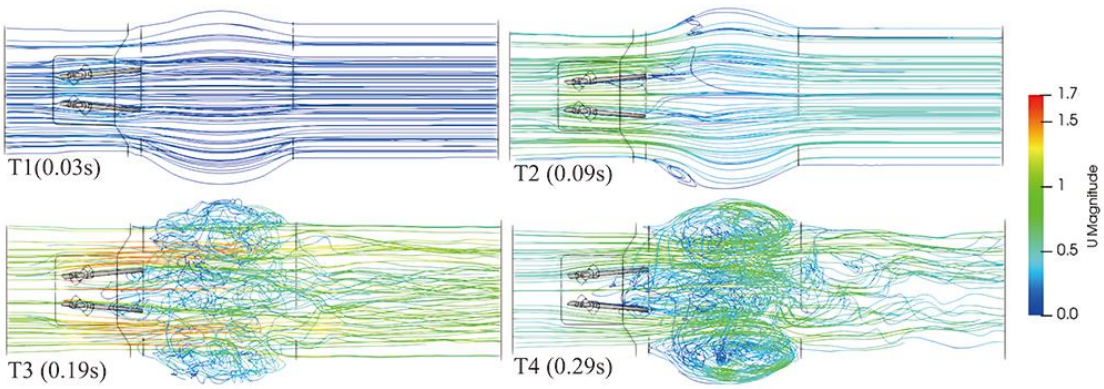

Figure 12. 3D-velocity streamlines of a simulation flow in the MHV (Newtonian model).

The velocity streamlines flowing through the hinge regions are shown in Figure 13. The streamlines enter the hinge recess via the gap between the leaflet flat surface and the housing. At the mid-acceleration phase (t = 0.09 s), the streamline appears to experience an obvious disturbance after passing through the hinge, and this disturbance area continues to grow in size with the increase in velocity; partially refluxed streamlines were also found at the peak velocity phase (t = 0.19 s). Velocity decreases over time and, at the mid-deceleration

phase (t = 0.29), the streamline forms a large annular vortex structure in the sinus region. The presence of low flow lines and large circular vortex structures increases the blood stagnation time, while the presence of high velocity jets can also be found around the hinge region. Both the increased blood standstill time and the presence of high velocity jets increase the risk of blood damage.

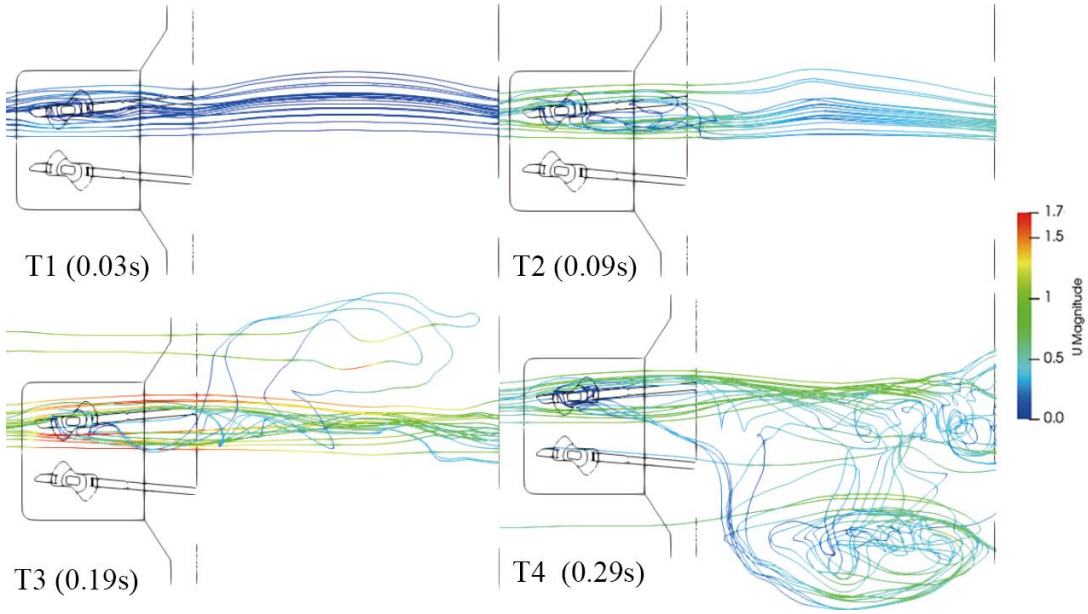

Figure 13. Velocity streamlines flowing through the hinge region (Newtonian model).

The amount and direction of velocity at the hinge recess are essential characteristics. However, the microflow should be carefully examined because it is the most significant component in thrombus formation and blood cell injury. The blood flows into the hinge regions creating a plane parallel to the hinge recess 0.14 mm away from the hinge recess floor. Figure 14 illustrates the velocity vector and the component contours. In this plane, the velocity vectors are also displayed to help comprehend the flow pattern in this tiny area. A lateral flow is generated in this region, primarily leading to vortices and stationary spots.

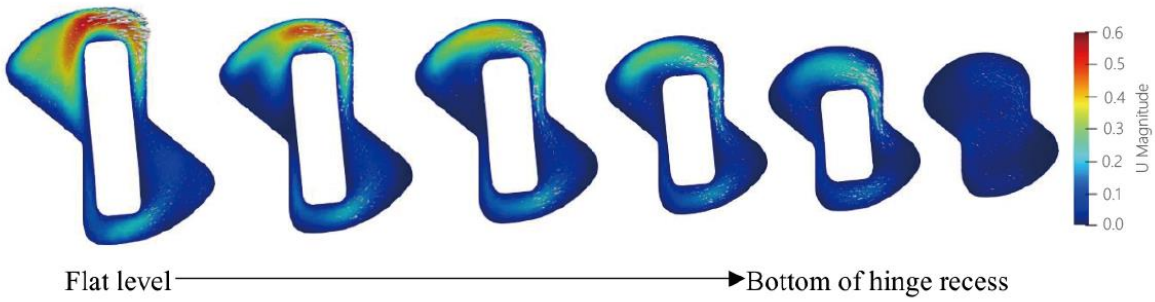

Figure 14. Variations of velocity profile with distance from the valve at the peak velocity phase (Newtonian model).

The adjacent corner (label a) has a region of increased velocity, and downstream of the corner is a region of significant swirling flow with a vertical velocity component. This flow characteristic results from the impact of the blood against the wall before it exits the coach's gap. The side angle produces strong axial flow (label b), but with a small out-of-plane velocity component. The blood may form a low-intensity backflow when passing through the gap between the surface of the leaflet ear and the bottom wall of the hinge region. The blood flow pattern can be observed by dividing the hinge

groove into six layers and analyzing the velocity vector and out-of-plane velocity at the different layers (Figure 15). Distinct velocity flows can be observed at different levels. Although the flat layer exhibits a larger forward flow pattern, a reverse velocity vector is still observed in the deepest layers.

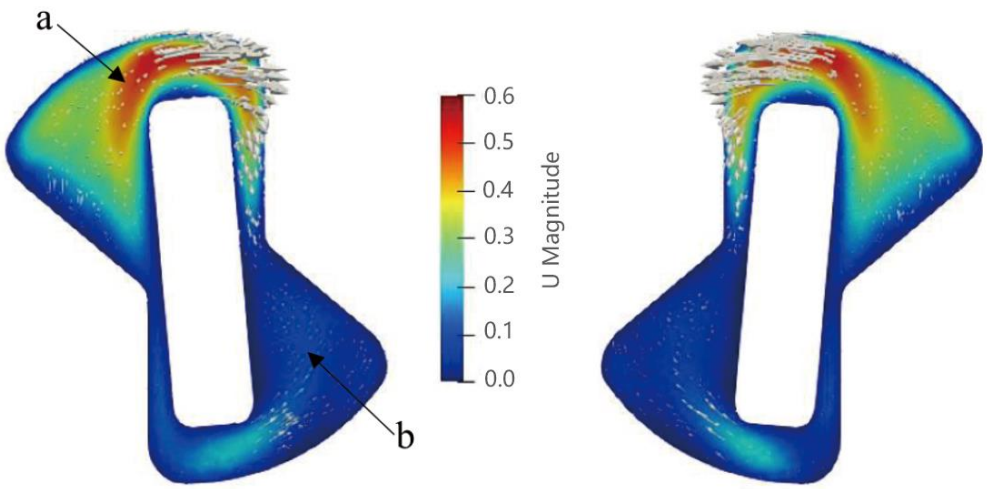

Figure 15. Peak velocity phase, velocity contours, and vector inside the hinge region in a plane with a distance of 0.15 mm from the hinged floor (a) adjacent corner; (b) side angle (Newtonian model).

Complex flow patterns and lower flow velocities at the hinge can increase residence time, blood cell aggregation, and cumulative damage, resulting in thrombosis and impaired hinge function.

3.2. Non-Newtonian Importance Factor

To investigate the impact of non-Newtonian shear-thinning models on WSS, the global non-Newtonian importance factor (I_G) is introduced. I_G is determined by calculating the average value of the relative difference between the viscosity and Newtonian values and expressed as a percentage. Thus, I_G is defined as Equation (4):

$$I_G = \frac{1}{N} \frac{\left(\sum_{i=1}^{N} (\mu - \mu_\infty)^2\right)^{0.5}}{\mu_\infty} \times 100 \tag{4}$$

where i is the wall grid number, including cells on the aortic wall and leaflet. N is the total number of grids, μ_∞ is the viscosity of Newtonian blood, and $\mu_\infty = 0.00345$ (kg/ms), and μ is the dynamic viscosity of blood. Table 2 lists the I_G values of all non-Newtonian models. All models display I_G values at T_1, which are higher than at other times. I_G decreases as blood flow accelerates, reaches a minimum at the peak of systole, and then gradually increases. Although blood flow has similar speeds at T_2 and T_4, I_G is different at these times. The blood flow pattern is more complicated at T_4, with the obvious jet flow and backflow. This depicts that the non-Newtonian effect of blood may change significantly during the blood pulsation cycle, and it is most pronounced during the deceleration phase.

Table 2. I_G at four time points.

I_G Calculated Time (s)		0.03	0.09	0.19	0.29
Carreau	WL	0.054	0.033	0.023	0.034
	HR	0.474	0.115	0.105	0.321
CY	WL	0.014	0.010	0.008	0.010
	HR	0.106	0.038	0.036	0.081

Table 2. *Cont.*

I_G Calculated Time (s)		0.03	0.09	0.19	0.29
Casson	WL	0.073	0.064	0.059	0.065
	HR	0.406	0.262	0.256	0.353
Md Casson	WL	0.039	0.026	0.017	0.025
	HR	0.338	0.085	0.075	0.254
Cross	WL	0.037	0.009	0.006	0.014
	HR	0.395	0.029	0.028	0.209
Md Cross	WL	0.059	0.037	0.026	0.038
	HR	0.505	0.131	0.120	0.340
K–L	WL	0.021	0.016	0.013	0.016
	HR	0.147	0.062	0.059	0.103
PL	WL	0.034	0.020	0.009	0.018
	HR	0.366	0.051	0.043	0.242
PE	WL	0.036	0.018	0.012	0.020
	HR	0.354	0.060	0.054	0.250
Md PE	WL	0.049	0.024	0.014	0.025
	HR	0.489	0.073	0.064	0.309

It is important to find the threshold of I_G by employing a procedure similar to that of Johnston et al. [7] in this study. When it flows above this value it can be regarded as a non-Newtonian flow. Johnston et al. concluded that $I_G = 0.25$ is the cut-off value of an important factor in the aorta, while Karimi et al. [2] concluded that the cut-off value is $I_G = 0.15$, the obtained WSS results.

Our study generates two different I_G values on the grid for all walls and the leaflet (WL) and the hinge region (HR). The cut-off value is obtained at $I_G = 0.05$ (WL) and $I_G = 0.25$ (HR) in our MHV model. In the MHV model domain, when $I_G < 0.05$, non-Newtonian models produce similar WSS to the Newtonian model. This method calculates the value in four-phase during the systole stage. Table 2 presents that the non-Newtonian viscosity model has a significant qualitative difference between the Carson and Newtonian models. However, the viscosity–shear rate of the Casson model varies closely. The power-law and the K–L models have lower I_G values than other non-Newtonian models. The calculation result of the critical factor can draw important conclusions: (a) The non-Newtonian viscosity model has a significant effect in the low-velocity stage and (b) the Casson and Newtonian models differ most significantly.

When narrowing the calculated domain to the hinge region, the cut-off value is defined as 0.25; when $I_G < 0.25$ in the hinge region, the maximum and average WSS difference is less than 3%. In the early accelerating phase (t = 0.03 s) and mid-decelerating phase (t = 0.29 s), most non-Newtonian models display different WSS results. We use different non-Newtonian models to depict the viscosity contours to better study the viscosity distribution inside the hinge region (Figure 16). The viscosity was higher near the leaflets. Moreover, the blood flow velocity was below the hinge region. In the early acceleration phase, the front of the leaflet ear exhibited high viscosity accumulation due to the increased velocity at the adjacent corners, while the front corners of the hinge exhibited a minor externally strong axial flow velocity component. A smaller velocity gradually moves to the back lateral corner at the mid-decelerating phase as the pulsatile flow changes. This flow distribution at adjacent corners may be due to the flow hitting the recess wall before leaving the hinge. The viscosity is high, particularly in the lateral corner. The contour illustrates that the Casson model viscosity is higher than other models, while the Cross and K–L model viscosity did not change significantly, and the value is approximate to Newtonian.

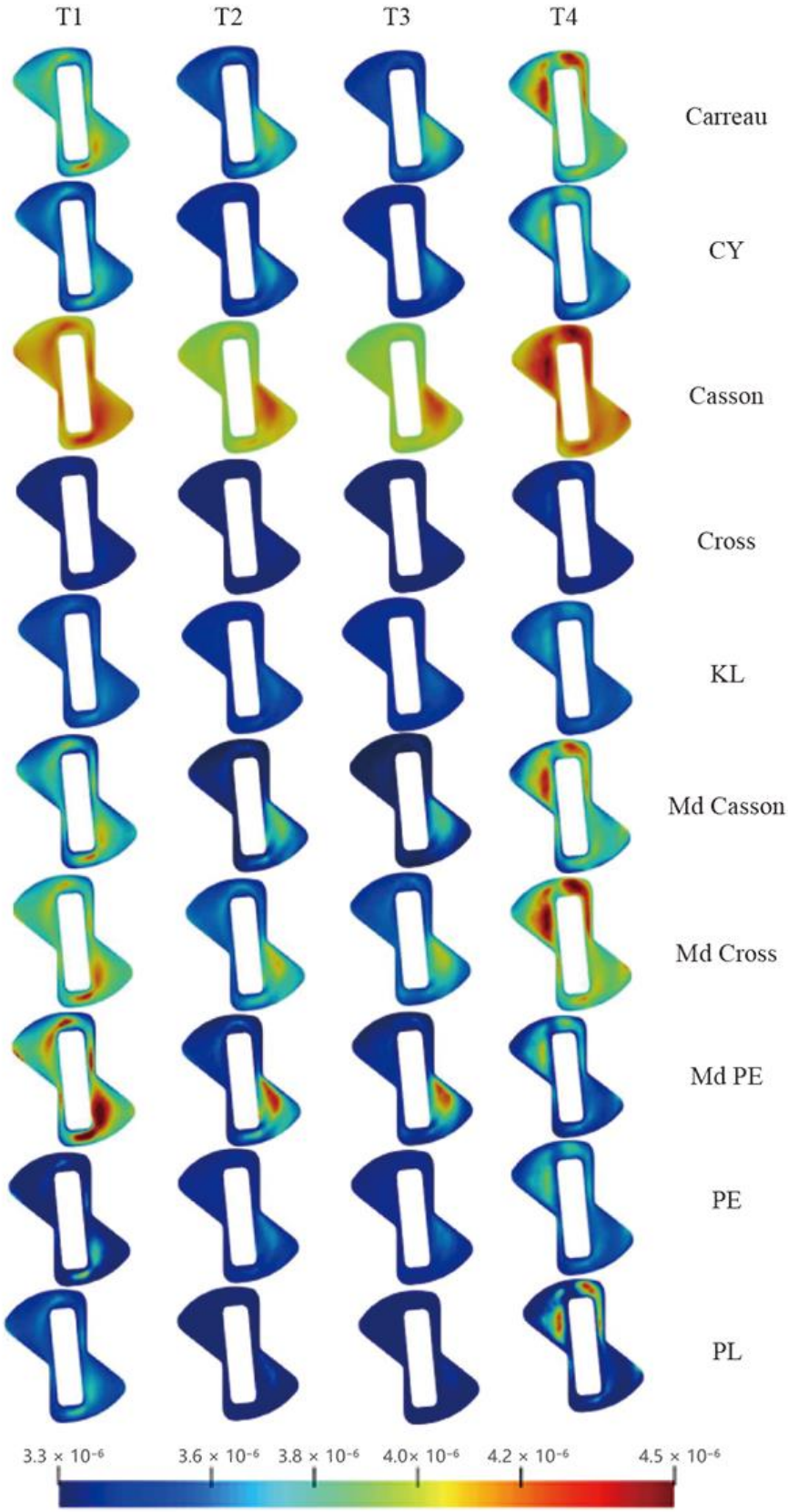

Figure 16. Viscosity contours of the hinge region for different non-Newtonian models.

3.3. Wall Shear Stress

This study investigated the impact of non-Newtonian viscosity models on WSS in pulsating blood flow. Additionally, we calculated the maximum and average values of WSS to evaluate the impact of non-Newtonian and Newtonian models on WSS in an MHV. In cardiovascular hemodynamics, a high WSS may damage red blood cells; therefore, a high WSS should be avoided whenever possible [48]. The WSS distribution in an MHV can be studied [49]. Table 3 shows the maximum and average values of the WSS on the wall and hinge regions. The average WSS agrees with the magnetic resonance imaging (MRI) data mean WSS in the ascending aorta, 8.6 (5.1–14.7) Pa, measured by Hellmeier F et al. [29]. The Newtonian fluids' maximum and average WSS are slightly smaller than those of non-Newtonian models. The Casson model produces the largest WSS at all stages, which is 70.34% higher than the Newtonian model at the early accelerating phase, and the average WSS difference is approximately 16.11%. The maximum WSS of the Modified Casson is 6.06% less than the Newtonian model. The maximum WSS of the Carreau, Carreau–Yasuda, Modified Casson, and Modified Cross is less than 2% of the Newtonian model, but the average WSS difference is greater than 5%. The large difference concentrates on the early accelerate and mid-decelerate phases. These results are consistent with the findings of Siamak et al. [9]. The maximum WSS of the Casson model is 60.89% higher than the Newtonian model.

Table 3. Maximum and average values of the WSS in an MHV.

Calculate Region		**Wall and Leaflet (Pa)**				**Hinge Region (Pa)**			
t (s)		**0.030**	**0.090**	**0.190**	**0.290**	**0.030**	**0.090**	**0.190**	**0.290**
Newtonian	Max_WSS	16.909	99.636	223.166	74.815	8.398	30.684	50.804	8.555
	Agv_WSS	2.043	6.483	13.840	5.908	1.412	6.587	8.220	1.283
Carreau	Max_WSS	17.147	101.630	227.185	76.133	8.080	31.633	49.959	8.994
	Agv_WSS	2.220	6.761	14.067	5.957	1.466	6.871	8.490	1.328
CY	Max_WSS	17.074	101.260	226.726	75.471	8.190	31.361	50.267	8.873
	Agv_WSS	2.149	6.654	13.987	5.891	1.443	6.763	8.381	1.324
Casson	Max_WSS	28.803	110.301	253.279	81.849	9.114	34.399	47.749	9.488
	Agv_WSS	2.372	7.281	14.923	6.012	1.514	7.386	9.132	1.399
Md Casson	Max_WSS	17.428	104.614	236.702	78.006	8.928	31.720	51.595	8.656
	Agv_WSS	2.171	6.514	14.069	6.015	1.462	6.611	8.234	1.349
Cross	Max_WSS	17.091	101.063	226.584	75.627	8.387	31.170	50.381	8.742
	Agv_WSS	2.083	6.572	13.954	5.736	1.422	6.678	8.305	1.273
Md Cross	Max_WSS	17.180	101.797	227.459	76.376	8.046	31.742	49.824	9.023
	Agv_WSS	2.244	6.802	14.105	6.020	1.475	6.912	8.533	1.342
K–L	Max_WSS	17.140	101.419	227.104	75.268	8.293	31.406	50.172	8.886
	Agv_WSS	2.134	6.661	14.020	5.874	1.438	6.766	8.400	1.348
PL	Max_WSS	17.067	101.089	226.558	75.586	8.754	31.193	50.318	8.893
	Agv_WSS	2.096	6.574	13.947	5.798	1.425	6.681	8.288	1.280
PE	Max_WSS	17.769	101.185	226.638	74.923	8.864	31.302	50.318	8.830
	Agv_WSS	2.134	6.628	13.970	5.836	1.539	6.738	8.353	1.397
Md PE	Max_WSS	17.066	101.223	226.640	75.288	8.183	31.346	50.297	8.886
	Agv_WSS	2.154	6.645	13.971	5.873	1.446	6.757	8.365	1.342

By narrowing the region to the hinge access, the difference of maximum WSS between non-Newtonian and Newtonian is greater than 4% at the early accelerate and mid-decelerate phases. The Casson model generates a maximum difference of approximately 12% among the Newtonian models. The calculated average WSS is higher in the hinge region of the non-Newtonian than the Newtonian model in all phases. However, the difference is insignificant when the blood flow through an MHV may suffer high cumulative stress.

The shear stress in the flow process may still affect the blood. When the threshold is exceeded, it is easy to cause blood damage. The threshold may be exceeded during the pulsating flow for only a short time. Simultaneously, the load and shear stress must be considered. Cumulative effects may include that ahigher average WSS means a higher accumulation of shear stress on the blood cells. The average WSS calculated by the Casson non-Newtonian model can be 17.6% higher than the Newtonian model during the initial acceleration phase. Modified Cross and Carreau models can be 9.8% and 8.7% higher, respectively. There is also a 5% difference for other models. Although the difference between Newtonian and non-Newtonian models decreases as blood flow velocity increases, the Newtonian hypothesis for blood may underestimate the effect of cumulative shear stress on blood cells. There is also a difference of around 5% for other models. The Casson model predicted the most significant WSS value, and Newtonian rheology predicted WSS values lower than other models. These results are consistent with previous studies. Non-Newtonian models improve the average WSS [30].

Figure 17 depicts the difference rate between the non-Newtonian and the Newtonian viscosity. The difference rate decreases as the speed increases during the contraction period. After the peak contraction, the different rate of WSS did not differ significantly from the previous one due to the strong secondary blood flow of the aortic arch during the deceleration period, consistent with the shear thinning characteristics of non-Newtonian blood. The non-Newtonian model had a higher viscosity and higher WSS than the Newtonian model at lower speeds and shear rates. At high shear rates, the non-Newtonian viscosity model shear-thinning viscosity gradually decreases, and the WSS difference also decreases as the viscosity approaches the Newtonian value. The WSS trends of other models are similar, except for the Casson model. The slight difference rate between the Cross and PL models indicates that their viscosity is close to the Newtonian model, and shear-thinning behavior is unclear. K–L and the modified Casson model are two modified and extended forms of the Casson model. The K–L and modified Casson models can better explain the shear-thinning behavior of blood over an extensive shear range [50].

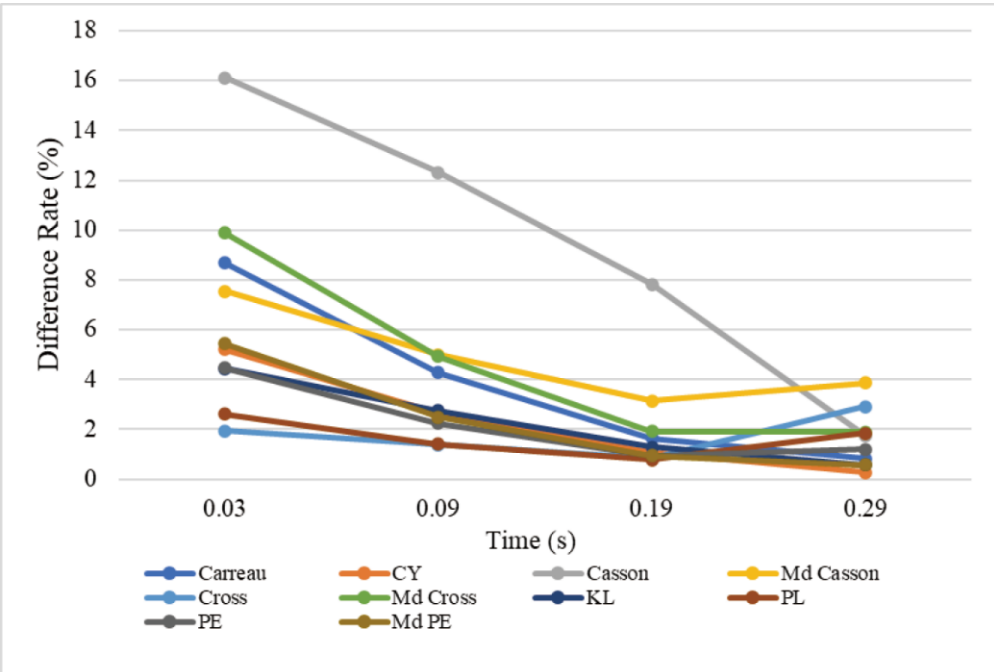

Figure 17. The rate of difference between non-Newtonian and Newtonian models.

Additionally, modified Cross, Carreau, CY, PE, and Modified PE can explain the shear-thinning of blood in an MHV. The low-velocity phase produces a higher viscosity; consequently, the mean WSS is greater than the Newtonian model. During the jet phase,

the blood is shear-thinned, and the non-Newtonian model viscosity tends toward the Newtonian model viscosity, allowing various models to approximate the mean WSS. The Modified Cross and Carreau models have apparent changes at different stages. WSS is higher in the low-velocity phase and similar to the Newtonian model around the peak phase. These two non-Newtonian models can replace the Newtonian model and better simulate the blood in an MHV.

Blood cells suffer prolonged damage due to the low velocity (high residence time), the low strain rate (high viscosity), and the relatively high mean WSS. Therefore, it can be expressed as the main thrombogenic part. The impact of the non-Newtonian flow model on hinge blood damage should be investigated further. These non-Newtonian model results are compared to the patient-specific model using other reference data, such as an MRI or particle image velocimetry (PIV).

4. Conclusions

In this study, we compared the effects of different non-Newtonian viscosity models on the hemodynamics of an MHV in an artery. The simulation geometry included the On-x MHV and the aorta, while the MHV model included the hinge regions to capture the impact of the geometry on the hemodynamic parameters. This study's primary objective was to compare the effects of different non-Newtonian models on MHV hemodynamics. The results revealed that non-Newtonian models influenced the MHV flow dynamics during the early to mid-phases, particularly in the hinge region. Numerical simulations indicated that different non-Newtonian viscosity models had higher local apparent viscosity values at the side angles of the lobular ears due to the low shear rate in the hinge area.

We also obtained the maximum and average values of WSS in different non-Newtonian viscosity models. The viscosity distribution of the Cross model differs significantly from other non-Newtonian models, particularly in its relatively consistent viscosity at high and low shear rates. The Casson model produces the highest WSS during the jet phase of the cardiac cycle at 253.3 Pa. This is approximately 30 Pa higher than the WSS produced by the Newtonian model. Other non-Newtonian models produce WSS values similar to the Casson model, with the difference between the two most pronounced in the hinge area. The Modified Cross and Carreau models exhibited significant changes in different stages of the cardiac cycle. Particularly, these models presented higher WSS values in the low-velocity phase and produced WSS results similar to the Newtonian model around the peak phase.

The partial optimization of the model during calculation can impact the accuracy of the results. The MHV should be placed in the artery of a specific patient in a real-world environment to obtain more realistic results. Additionally, the current non-Newtonian blood model only considers shear-thinning characteristics and does not account for blood thixotropy and viscoelastic properties. Future studies will focus on addressing these limitations.

Author Contributions: Conceptualization, A.C. and A.A.B.; methodology, A.C.; software, A.C. and A.A.B.; validation, N.B.I., A.C. and K.A.A.; formal analysis, A.C. and A.A.B.; investigation, N.B.I.; resources, N.B.I. and K.A.A.; data curation, A.C.; writing—original draft preparation, A.C.; writing—review and editing, by all authors; visualization, A.C. and N.B.I.; supervision, K.A.A.; project administration, K.A.A. All authors have read and agreed to the published version of the manuscript.

Funding: This research received no external funding.

Data Availability Statement: The figures and tables used to support the findings of this study are included in the article.

Acknowledgments: The authors would like to express their sincere gratitude to the Department of Aerospace Engineering and the Department of Mechanical Engineering, Faculty of Engineering, Universiti Putra Malaysia, for their close cooperation with this work. The authors also thank the supervisor and co-supervisor for their help.

Conflicts of Interest: The authors declare no conflict of interest.

References

1. World Health Organization. Cardiovascular Diseases (cvds). 2019. Available online: http://www.who.int/mediacentre/factsheets/fs317/en/index.html (accessed on 7 February 2019).
2. Smadi, O.; Hassan, I.; Pibarot, P.; Kadem, L. Numerical and experimental investigations of pulsatile blood flow pattern through a dysfunctional mechanical heart valve. *J. Biomech.* **2010**, *43*, 1565–1572. [CrossRef]
3. Emery, R.W.; Mettler, E.G.O.N.; Nicoloff, D.M. A new cardiac prosthesis: The St. Jude Medical cardiac valve: In vivo results. *Circulation* **1979**, *60*, 48–54. [CrossRef] [PubMed]
4. Gott, V.L.; Alejo, D.E.; Cameron, D.E. Mechanical heart valves: 50 years of evolution. *Ann. Thorac. Surg.* **2003**, *76*, S2230–S2239. [CrossRef] [PubMed]
5. Shahriari, S.; Maleki, H.; Hassan, I.; Kadem, L. Evaluation of shear stress accumulation on blood components in normal and dysfunctional bileaflet mechanical heart valves using smoothed particle hydrodynamics. *J. Biomech.* **2012**, *45*, 2637–2644. [CrossRef] [PubMed]
6. Bessonov, N.; Sequeira, A.; Simakov, S.; Vassilevskii, Y.; Volpert, V. Methods of blood flow modelling. *Math. Model. Nat. Phenom.* **2016**, *11*, 1–25. [CrossRef]
7. Johnston, B.M.; Johnston, P.R.; Corney, S.; Kilpatrick, D. Non-Newtonian blood flow in human right coronary arteries: Steady state simulations. *J. Biomech.* **2004**, *37*, 709–720. [CrossRef]
8. Smadi, O.; Fenech, M.; Hassan, I.; Kadem, L. Flow through a defective mechanical heart valve: A steady flow analysis. *Med. Eng. Phys.* **2009**, *31*, 295–305. [CrossRef]
9. Arzani, A. Accounting for residence-time in blood rheology models: Do we really need non-Newtonian blood flow modelling in large arteries? *J. R. Soc. Interface* **2018**, *15*, 20180486. [CrossRef]
10. Berger, S.A.; Jou, L.D. Flows in stenotic vessels. *Annu. Rev. Fluid Mech.* **2000**, *32*, 347–382. [CrossRef]
11. Merrill, E.W.; Gilliland, E.R.; Margetts, W.G.; Hatch, F.T. Rheology of human blood and hyperlipemia. *J. Appl. Physiol.* **1964**, *19*, 493–496. [CrossRef]
12. Phillips, W.M.; Deutsch, S. Toward a constitutive equation for blood. *Biorheology* **1975**, *12*, 383–389. [CrossRef] [PubMed]
13. Yun, B.M.; McElhinney, D.B.; Arjunon, S.; Mirabella, L.; Aidun, C.K.; Yoganathan, A.P. Computational simulations of flow dynamics and blood damage through a bileaflet mechanical heart valve scaled to pediatric size and flow. *J. Biomech.* **2014**, *47*, 3169–3177. [CrossRef] [PubMed]
14. Yeh, H.H.; Barannyk, O.; Grecov, D.; Oshkai, P. The influence of hematocrit on the hemodynamics of artificial heart valve using fluid-structure interaction analysis. *Comput. Biol. Med.* **2019**, *110*, 79–92. [CrossRef] [PubMed]
15. Campo-Deaño, L.; Dullens, R.P.; Aarts, D.G.; Pinho, F.T.; Oliveira, M.S. Viscoelasticity of blood and viscoelastic blood analogues for use in polydymethylsiloxane in vitro models of the circulatory system. *Biomicrofluidics* **2013**, *7*, 034102. [CrossRef]
16. Zupančič Valant, A.; Žiberna, L.; Papaharilaou, Y.; Anayiotos, A.; Georgiou, G.C. The influence of temperature on rheological properties of blood mixtures with different volume expanders—Implications in numerical arterial hemodynamics simulations. *Rheol. Acta* **2011**, *50*, 389–402. [CrossRef]
17. De Vita, F.; De Tullio, M.D.; Verzicco, R. Numerical simulation of the non-Newtonian blood flow through a mechanical aortic valve. *Theor. Comput. Fluid Dyn.* **2016**, *30*, 129–138. [CrossRef]
18. Moradicheghamahi, J.; Sadeghiseraji, J.; Jahangiri, M. Numerical solution of the Pulsatile, non-Newtonian and turbulent blood flow in a patient specific elastic carotid artery. *Int. J. Mech. Sci.* **2019**, *150*, 393–403. [CrossRef]
19. Doost, S.N.; Zhong, L.; Su, B.; Morsi, Y.S. The numerical analysis of non-Newtonian blood flow in human patient-specific left ventricle. *Comput. Methods Programs Biomed.* **2016**, *127*, 232–247. [CrossRef]
20. Nadarajah, S.K.; McMullen, M.S.; Jameson, A. Aerodynamic shape optimization for unsteady three-dimensional flows. *Int. J. Comput. Fluid Dyn.* **2006**, *20*, 533–548. [CrossRef]
21. Weddell, J.C.; Kwack, J.; Imoukhuede, P.I.; Masud, A. Hemodynamic analysis in an idealized artery tree: Differences in wall shear stress between Newtonian and non-Newtonian blood models. *PLoS ONE* **2015**, *10*, e0124575. [CrossRef]
22. Caballero, A.D.; Laín, S. Numerical simulation of non-Newtonian blood flow dynamics in human thoracic aorta. *Comput. Methods Biomech. Biomed. Eng.* **2015**, *18*, 1200–1216. [CrossRef] [PubMed]
23. Hanafizadeh, P.; Mirkhani, N.; Davoudi, M.R.; Masouminia, M.; Sadeghy, K. Non-newtonian blood flow simulation of diastolic phase in bileaflet mechanical heart valve implanted in a realistic aortic root containing coronary arteries. *Artif. Organs* **2016**, *40*, E179–E191. [CrossRef] [PubMed]
24. Abbas, S.S.; Nasif, M.S.; Al-Waked, R.; Meor Said, M.A. Numerical investigation on the effect of bileaflet mechanical heart valve's implantation tilting angle and aortic root geometry on intermittent regurgitation and platelet activation. *Artif. Organs* **2020**, *44*, E20–E39. [CrossRef] [PubMed]
25. Choi, C.R.; Kim, C.N. Analysis of blood flow interacted with leaflets in MHV in view of fluid-structure interaction. *KSME Int. J.* **2001**, *15*, 613–622. [CrossRef]
26. Kadhim, S.K.; Nasif, M.S.; Al-Kayiem, H.H.; Al-Waked, R. Computational fluid dynamics simulation of blood flow profile and shear stresses in bileaflet mechanical heart valve by using monolithic approach. *Simulation* **2018**, *94*, 93–104. [CrossRef]
27. Forsyth, A.M.; Wan, J.; Owrutsky, P.D.; Abkarian, M.; Stone, H.A. Multiscale approach to link red blood cell dynamics, shear viscosity, and ATP release. *Proc. Natl. Acad. Sci. USA* **2011**, *108*, 10986–10991. [CrossRef]

28. Wagner, C.; Steffen, P.; Svetina, S. Aggregation of red blood cells: From rouleaux to clot formation. *Comptes Rendus Phys.* **2013**, *14*, 459–469. [CrossRef]
29. Hellmeier, F.; Nordmeyer, S.; Yevtushenko, P.; Bruening, J.; Berger, F.; Kuehne, T.; Goubergrits, L.; Kelm, M. Hemodynamic evaluation of a biological and mechanical aortic valve prosthesis using patient-specific MRI-based CFD. *Artif. Organs* **2018**, *42*, 49–57. [CrossRef]
30. Karimi, S.; Dabagh, M.; Vasava, P.; Dadvar, M.; Dabir, B.; Jalali, P. Effect of rheological models on the hemodynamics within human aorta: CFD study on CT image-based geometry. *J. Non Newton. Fluid Mech.* **2014**, *207*, 42–52. [CrossRef]
31. Jahangiri, M.; Saghafian, M.; Sadeghi, M.R. Numerical simulation of non-Newtonian models effect on hemodynamic factors of pulsatile blood flow in elastic stenosed artery. *J. Mech. Sci. Technol.* **2017**, *31*, 1003–1013. [CrossRef]
32. Jahangiri, M.; Saghafian, M.; Sadeghi, M.R. Numerical study of turbulent pulsatile blood flow through stenosed artery using fluid-solid interaction. *Comput. Math. Methods Med.* **2015**, *2015*, 515613. [CrossRef] [PubMed]
33. Yin, W.; Gallocher, S.; Pinchuk, L.; Schoephoerster, R.T.; Jesty, J.; Bluestein, D. Flow-induced platelet activation in a St. Jude mechanical heart valve, a trileaflet polymeric heart valve, and a St. Jude tissue valve. *Artif. Organs* **2005**, *29*, 826–831. [CrossRef] [PubMed]
34. Mirkhani, N.; Davoudi, M.R.; Hanafizadeh, P.; Javidi, D.; Saffarian, N. On-X heart valve prosthesis: Numerical simulation of hemodynamic performance in accelerating systole. *Cardiovasc. Eng. Technol.* **2016**, *7*, 223–237. [CrossRef] [PubMed]
35. De Tullio, M.D.; Cristallo, A.; Balaras, E.; Verzicco, R. Direct numerical simulation of the pulsatile flow through an aortic bileaflet mechanical heart valve. *J. Fluid Mech.* **2009**, *622*, 259–290. [CrossRef]
36. Akutsu, T.; Matsumoto, A. Influence of three mechanical bileaflet prosthetic valve designs on the three-dimensional flow field inside a simulated aorta. *J. Artif. Organs* **2010**, *13*, 207–217. [CrossRef]
37. Onel, H.C.; Tuncer, I.H. A comparative study of wake interactions between wind-aligned and yawed wind turbines using LES and actuator line models. *J. Phys. Conf. Ser.* **2020**, *1618*, 062009. [CrossRef]
38. Zakaria, M.S.; Ismail, F.; Tamagawa, M.; Aziz, A.F.A.; Wiriadidjaja, S.; Basri, A.A.; Ahmad, K.A. Review of numerical methods for simulation of mechanical heart valves and the potential for blood clotting. *Med. Biol. Eng. Comput.* **2017**, *55*, 1519–1548. [CrossRef]
39. O'Callaghan, S.; Walsh, M.; McGloughlin, T. Numerical modelling of Newtonian and non-Newtonian representation of blood in a distal end-to-side vascular bypass graft anastomosis. *Med. Eng. Phys.* **2006**, *28*, 70–74. [CrossRef]
40. Kim, S.K. Collective viscosity model for shear thinning polymeric materials. *Rheol. Acta* **2020**, *59*, 63–72. [CrossRef]
41. Cho, Y.I.; Kensey, K.R. Effects of the non-Newtonian viscosity of blood on flows in a diseased arterial vessel. Part 1: Steady flows. *Biorheology* **1991**, *28*, 241–262. [CrossRef]
42. Shibeshi, S.S.; Collins, W.E. The rheology of blood flow in a branched arterial system. *Appl. Rheol.* **2005**, *15*, 398–405. [CrossRef] [PubMed]
43. Borazjani, I.; Ge, L.; Sotiropoulos, F. Curvilinear immersed boundary method for simulating fluid structure interaction with complex 3D rigid bodies. *J. Comput. Phys.* **2008**, *227*, 7587–7620. [CrossRef] [PubMed]
44. Simon, H.A.; Ge, L.; Sotiropoulos, F.; Yoganathan, A.P. Simulation of the three-dimensional hinge flow fields of a bileaflet mechanical heart valve under aortic conditions. *Ann. Biomed. Eng.* **2010**, *38*, 841–853. [CrossRef] [PubMed]
45. Prakash, S.; Ethier, C.R. Requirements for mesh resolution in 3D computational hemodynamics. *J. Biomech. Eng.* **2001**, *123*, 134–144. [CrossRef] [PubMed]
46. Grigioni, M.; Daniele, C.; D'Avenio, G.; Barbaro, V. The influence of the leaflets' curvature on the flow field in two bileaflet prosthetic heart valves. *J. Biomech.* **2001**, *34*, 613–621. [CrossRef]
47. Khalili, F.; Gamage, P.; Sandler, R.H.; Mansy, H.A. Adverse hemodynamic conditions associated with mechanical heart valve leaflet immobility. *Bioengineering* **2018**, *5*, 74. [CrossRef]
48. Ge, L.; Jones, S.C.; Sotiropoulos, F.; Healy, T.M.; Yoganathan, A.P. Numerical simulation of flow in mechanical heart valves: Grid resolution and the assumption of flow symmetry. *J. Biomech. Eng.* **2003**, *125*, 709–718. [CrossRef]
49. Smadi, O.; Garcia, J.; Pibarot, P.; Gaillard, E.; Hassan, I.; Kadem, L. Accuracy of Doppler-echocardiographic parameters for the detection of aortic bileaflet mechanical prosthetic valve dysfunction. *Eur. Heart J. Cardiovasc. Imaging* **2014**, *15*, 142–151. [CrossRef]
50. Zhang, J.B.; Kuang, Z.B. Study on blood constitutive parameters in different blood constitutive equations. *J. Biomech.* **2000**, *33*, 355–360. [CrossRef]